Electroluminescence and Dark Lock-In Thermography for the Quality Assessment of Metal-Wrap-Through Solar Devices

Ruggeri, Edoardo; van Aken, Bas; Isabella, Olindo; Zeman, Miro

DOI
10.1109/JPHOTOV.2018.2850530

Publication date
2018

Document Version
Accepted author manuscript

Published in
IEEE Journal of Photovoltaics

Electroluminescence and Dark Lock-In Thermography for the Quality Assessment of Metal-Wrap-Through Solar Devices

Edoardo Ruggeri, Bas B. Van Aken, Olindo Isabella, and Miro Zeman

***Abstract*—Imaging techniques, like electroluminescence and dark lock-in thermography, are valuable quality control tools as they yield quantitative and spatially resolved information about the device. In this paper, we isolated some of the conductive foil–cell interconnections of back-contact solar cells to study the appearance of these intentional failures in electroluminescence, dark lock-in thermography, and series resistance images. It has been found that isolated emitter-to-foil contacts are clearly visible in the three imaging techniques, as they show characteristic features that deviate from the features typical of functioning emitter-to-foil dots. Isolated base-to-foil contacts are instead invisible in the images obtained by electroluminescence and only hardly visible in the images obtained by the other two techniques. Only after a large amount of contacts are isolated, a local current redistribution or drastic series resistance increase is noticeable. Two graphical methods for the automatic identification of isolated emitter-to-foil contacts in electroluminescence, dark lock-in thermography, and series resistance images were also designed, showing a success rate of 97% in the investigated cells. Such techniques could represent useful tools for implementation in inline quality control processes. Moreover, the techniques and conclusions drawn in this paper can be extended to a large number of other conventional and emerging photovoltaic technologies.**

***Index Terms*—Electrical resistance measurement, electroluminescence, failure analysis, infrared imaging, radiation imaging, solar energy.**

I. Introduction

SOLAR power is becoming an attractive energy-generation solution for households as well as larger power plants owing to its exponentially decreasing cost. This fact is further reinforced as the installed capacity worldwide exponentially grows. With the increasing rate of users relying on solar-generated electricity, ensuring the quality and correcting the functionality of solar devices have become imperative tasks for photovoltaic companies. In fact, quality control on production batches must be effectively performed not to hinder throughput with excessively long methods of investigation. Highly efficient, effective, and reliable quality control methods are therefore a necessity for any modern company producing photovoltaic devices [1], [2].

Currently, the most common kind of solar module electrical quality control is the current–voltage (*IV*) curve analysis. It involves the tracing of the full *IV* curve of either all of the solar devices produced or of a representative sample of the production batch. Usually, two or more *IV* curves under different irradiation conditions are traced for each module, such that the short-circuit current I_{sc}, open-circuit voltage V_{oc}, fill factor FF, efficiency η as well the reverse saturation current, module resistance, temperature coefficients, and ideality factor parameters can be extracted and compared with the relevant standards. This method, whereas widely used, has some limitations. Its biggest shortcoming resides in the fact that although it allows the extraction of a number of key electrical parameters, which are most certainly good indicators of the electrical validity of a specific device, it cannot give information regarding the potential physical defects of the cells, the homogeneity of the material, the active and inactive areas of the cell, and other defects such as broken metallization lines or local shunts. This is especially true in the case of defects such as degrading fingers or deteriorating contact dots in metal-wrap-through (MWT) solar cells. These defects in fact tend to introduce only negligible variations in *IV* data until they reach severe stages of degradation and cannot therefore be detected via quality controls relying on *IV* data [3]–[7]. Imaging techniques such as electroluminescence (EL) and dark lock-in thermography (DLIT) can provide valuable complementary techniques to support *IV* data investigations. Whereas *IV* investigations provide insights into the overall performance of the device, these imaging techniques enable visualizing the defect locations within each cell and determine their nature: broken metallization, shunt, crack, etc. These imaging techniques can also yield mappings of electrical parameters, such as local current, voltage, and carrier lifetime via a moderate amount of postprocessing. Furthermore, they are fast and do not require expensive equipment to be carried out, which further strengthens their feasibility for the integration into inline quality assurance protocols [7]–[11]. In this paper, we study the effects of intentionally broken contact dots in p-type

Manuscript received March 18, 2018; revised May 17, 2018; accepted May 27, 2018. *(Corresponding author: Edoardo Ruggeri.)*

E. Ruggeri was with the Photovoltaic Materials and Devices Group, Delft University of Technology, Delft 2628 CD, The Netherlands and also with the Solar Energy Department, ECN part of TNO, Petten 1755 LE, The Netherlands. He is now with the Optoelectronics Group, Cavendish Laboratory, University of Cambridge, Cambridge CB3 0HE, U.K. (e-mail: edoardoruggeri1@gmail.com).

B. B. Van Aken is with the Solar Energy Department, ECN part of TNO, Petten 1755 LE, The Netherlands (e-mail: bas.vanaken@tno.nl).

O. Isabella and M. Zeman are with the Photovoltaic Materials and Devices Group, Delft University of Technology, Delft 2628 CD, The Netherlands (e-mail: o.isabella@tudelft.nl; m.zeman@tudelft.nl).

Color versions of one or more of the figures in this paper are available online at http://ieeexplore.ieee.org.

Digital Object Identifier 10.1109/JPHOTOV.2018.2850530

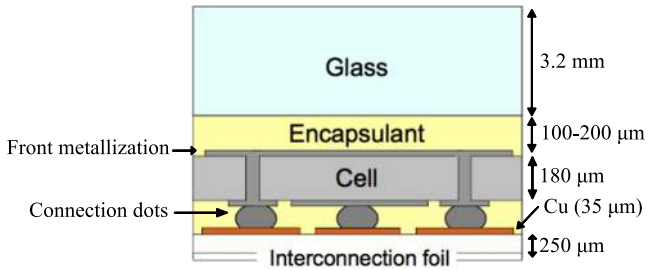

Fig. 1. Cross-sectional explicative sketch of the MWT module. Cells are p-type, Al-BSF with emitter on glass side and base and Al-BSF on interconnection side. The methodology as presented here is applicable to all interconnection schemes involving contact points or small contact areas.

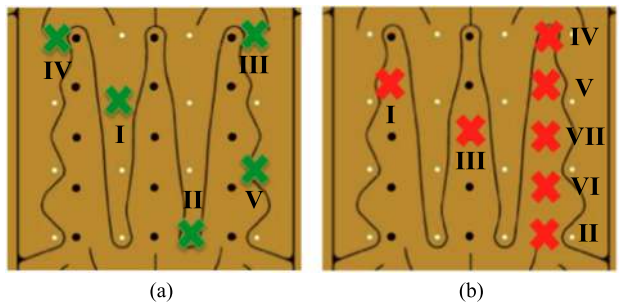

Fig. 2. Contact dots isolation patterns in the two investigated cells (shown: last isolation step). (a) Isolated emitter dots. (b) Isolated base dots.

multicrystalline silicon MWT solar devices developed at the Energy Research Centre of The Netherlands using electroluminescence, dark lock-in thermography, and the resulting post-processed series resistance distribution images [12]. The aim is threefold

1) determining how purposely isolated contact dots appear in these images;
2) what their behavior is;
3) demonstrating that quality control relying on EL, DLIT, and series resistance images is more reliable than quality control relying solely on IV data.

II. Experimental Methodology

A. Metal-Wrap-Through Technology

MWT cells are designed to minimize the front-contact shading losses while achieving the same or potentially higher efficiencies than conventional front metallization technologies. The front fingers are connected to silver contact dots punching through the wafer, connecting the front emitter layer to the back contact of the cell, a copper foil (emitter-to-foil contact dots, to be hereafter referred to as emitter dots). Between the back contact and the base layer, an aluminum back surface field (Al-BSF) is placed. Also the base layer is provided with silver contact dots, connecting the base layer to the back contact (base-to-foil contact dots, to be hereafter referred to as base dots). Fig. 1 shows the cross section of an MWT device, where the position of the emitter and base dots as well as all the interconnections is visible. Physical separation between the emitter and base side of the back-contact copper foil to avoid short-circuiting of the cell is achieved via etching of the copper foil. This is visible in Fig. 2, showing the back contacting pattern of MWT solar cells, where the white dots are the emitter dots, the black dots are the base dots, and the black wavy pattern travelling across the cell is the etched trench in the copper foil.

B. Introduction of Defects

To carry out the investigations, two encapsulated MWT solar cells (i.e., mini-modules resembling Fig. 1) have been used. In order to simulate malfunctioning contacts, a number of contact dots have been manually isolated one-by-one in each cell. This was achieved by drilling away the back-contact copper sheet around them. In one cell, only some emitter dots were deliberately isolated (hereinafter referred as emitter dots-only cell), whereas in the other, only some base dots (hereinafter referred as base dots-only cell). The location of the isolated contact dots in the two cells was chosen such as to simulate random failure. In different subsequent steps, up to five emitter dots were isolated in one case, whereas in the other case two additional base dots were isolated to more clearly visualize the effects of failing base dots. Moreover, in the latter cell, the locations of the last steps were chosen to lead to an entirely isolated vertical row of base dots. This too was done to better visualize the effects of failing base dots. The patterns of the isolated contact dots in the two cells are shown in Fig. 2(a) and (b), with roman numbers showing the temporal order of dot failure.

C. Electroluminescence Imaging

Electroluminescence Imaging (EL) imaging involves the capturing of the EL radiation emitted by solar cells under forward bias as a result of radiative recombination [13]–[15]. EL images were taken at each step from the front of the cells using a Nikon D700 camera with a 14-bit CMOS sensor. A “hot mirror” reflecting away wavelengths larger than 750 nm is usually placed in front of conventional camera sensors in order to minimize infrared light contamination of the images. In this setup, the mirror was removed such as to capture the infrared EL radiation emitted from the devices. The forward bias was achieved via an autoranging Delta Elektronika SM 7020-D power supply. Both the camera and the module were placed in a dark room. The Nikon camera was connected to a computer to process the images. The devices were tested under two conditions: low forward bias at 0.1 I_{sc} (0.8 A) and high forward bias at I_{sc} (8 A). All images were taken with an exposure time of 30 s. High forward bias imaging allows the imaging of series-resistance-dependent and independent defects and of other series resistance effects, whereas low bias imaging allows preferential imaging of series-resistance-independent defects by minimizing series resistance effects. The two images can then be postprocessed to visualize a voltage mapping of the cell. This is achieved by means of the model developed by Haunschild *et al.* [16], as the local emission EL intensity scales exponentially with the local effective junction voltage. The precise operating voltage and current of the cells was recorded via multimeters to derive a local voltage drop image mapping by subtracting the local voltage value from the operating voltage at every pixel of the image [16]–[20].

D. Dark Lock-In Thermography

DLIT is an imaging technique involving the capturing of the emitted infrared thermal radiation from cells under the application of a forward bias. DLIT is effectively a mapping of the locally dissipated power [21]. DLIT images of the two cells were taken at each isolation step from the back of the cells using a FLIR SC655 camera provided with an uncooled focal plane array sensor in the 7.5–13 μm range, capable of delivering a frame rate of 50 Hz at full-frame resolution. The camera was connected to a computer equipped with IrNDT software by Automation Technologies, which allows for camera control, image capture, and data collection and analysis. The power supply was a Kepco BOP 72-14 MG and it was connected to a National Instruments SC-2345 signal-conditioning unit, in turn connected to the computer. With DLIT technique a number of images can be carried out, but the amplitude images are most relevant for the investigations reported in this paper, as they combine high spatial resolution to reasonably proportional approximations of the locally dissipated power (in fact, only the S^{-90° image is directly proportional to the locally dissipated power, but it displays very poor spatial resolution) [21]. Power images were thereby derived from them. As in the EL case, the cells were tested under a forward bias of 8 A and with an exposure time of 30 min to optimize signal-to-noise ratio. A frequency of 0.2 Hz was set to allow extended heat sources imaging. The precise operating voltage and current of the cells were recorded via multimeters, to derive a mapping of the locally dissipated power via the model developed by Breitenstein *et al.* [21], [22]. The power dissipation images can be further postprocessed by dividing them by the local absolute voltage EL image taken at the same 8 A forward bias conditions, thereby obtaining a local current distribution image [10], [21].

E. Series Resistance Imaging

The series resistance distribution map is derived via the recombination current and series resistance imaging (RESI) method [10]. The method involves dividing the local voltage drop EL image by the local current DLIT image taken at the same 8 A forward bias condition, thereby obtaining the local series resistance value at every pixel of the image. In order to satisfy these conditions, the EL and DLIT images have been captured at the same ambient conditions.

F. IV Testing

To track the changes in electrical parameters, *IV* readings have been taken after each step using a Pasan 3B solar simulator.

III. Results and Discussion

Table I summarizes the defect-free electrical parameters of the two investigated cells, where "ED" identifies the cell in which only emitter dots were isolated and "BD" the cell in which only base dots were isolated. In their initial stage, the cells performed very similarly.

TABLE I
ELECTRICAL PARAMETERS OF THE TWO CELLS DERIVED FROM IV TRACING INVESTIGATION PRIOR ISOLATION STEPS

Parameter	ED	BD
I_{sc} [A]	8.76	8.78
V_{oc} [V]	0.628	0.629
FF [%]	75.3	75.3
η [%]	17.0	17.1

ED and BD stand for emitter dots and base dots cells, respectively.

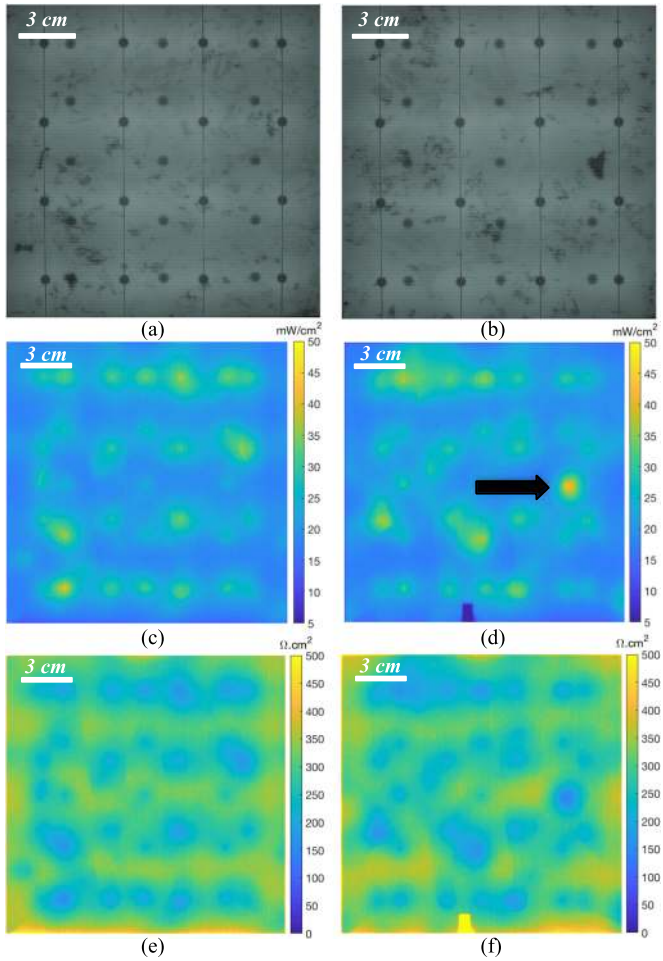

Fig. 3. EL, DLIT, and RESI images after step 0 of the two investigated cells. (a) EL ED. (b) EL BD. (c) DLIT ED. (d) DLIT BD. (e) RESI ED. (f) RESI BD.

A. Imaging Investigation

The presented images have been selected to show the progression of intentionally induced degradation and support the findings that the degradation is more confidently detected by EL, DLIT, and RESI images than with *IV* data. In the following images, white-circled dots indicate isolated emitter dots, whereas black-circled dots indicate isolated base dots.

1) Defect-Free Cells: The EL, DLIT, and RESI images of the two cells in their initial as-fabricated stage (i.e., without any deliberately isolated contact dots, step 0) are presented in Fig. 3(a)–(f). In EL images (reported in a.u.), the bright-

ness of each pixel is directly proportional to the intensity of emitted EL radiation, whereas in DLIT power images, the brightness of each pixel is approximately proportional to the locally dissipated power (i.e., the product of local voltage and local current), where darker blue areas indicate areas of low power dissipation and brighter (yellow, white) areas indicate areas of high power dissipation. In RESI images, darker blue areas indicate areas of low series resistance and brighter green-to-yellow areas indicate areas of high series resistance.

From the figures, it is possible to observe the patterns of the contact dots as well as the crystallographic defects and inhomogeneities spread across the entire area of the solar cell. In EL and RESI imaging, the areas of crystallographic anomalies appear darker due to the larger rates of nonradiative recombination at those sites. In DLIT imaging they instead appear brighter as a result of the large amount of power dissipated within them. The black arrow in Fig. 3(d) indicates an exemplary crystallographic defect appearing bright in DLIT and dark in EL and RESI. Note that the dark area at the bottom of Fig. 3(d) and (f) is caused by one of the external contacts.

It can be observed that the emitter dots, arranged in odd vertical lines, show bright halos surrounding them in both EL and DLIT images, denoting higher current densities, junction voltages, and dissipated power. In RESI images, they instead appear darker, as the series resistance is low within and in the areas surrounding them. In EL images, the front-side emitter dots are clearly visible darker circles, as the front metallization blocks the EL light, while in DLIT images they are visible as point-shaped areas of respectively high and low brightness that extend beyond the actual size of the contact. From the RESI figures, it is also observed that the series resistance increases with the distance from the base and emitter contacts. This is expected, as the dots have the highest quality electrical contact, whereas series resistance losses within the front metallization grid, the Al-BSF, and the silicon increase moving further away from the emitter and base dots.

Base dots do not show halos in EL images such as emitter dots do, as the signal of the latter greatly overshadows the one of the former. In fact, whereas the front-side emitter dots are clearly visible darker circles, the rear-side base dots are not directly imaged. The dark circles on the images corresponding to their position on the cell's rear side are due to lower EL intensity as the Al-BSF is not present at these locations, therefore leading to higher local recombination rates. In DLIT images, base dots are still visible as high brightness spots extending beyond the actual size of the contact, as they conduct current and therefore dissipate power. Base dots are also imaged in RESI images as low brightness spots, but their contrast with respect to their surroundings is much lower than in the DLIT images, as RESI images are a combination of EL and DLIT images.

2) Emitter Dots Isolation: The EL, DLIT, and RESI images of the emitter dots-only cell at step 2 of the sequence of emitter dots isolation are shown in Fig. 4(a)–(c). The white circles show the isolated emitter dots. In Fig. 4(a), it is observed that the bright halo surrounding the connected dots is absent at the isolated emitter dots in EL imaging, indicating areas of lower current

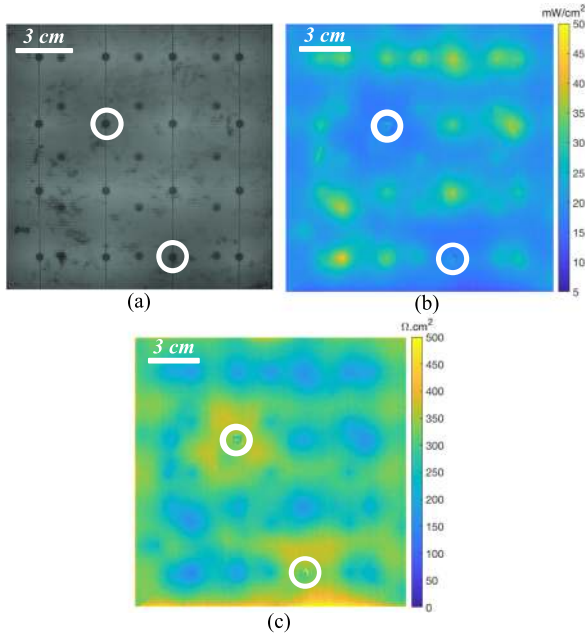

Fig. 4. (a) EL, (b) DLIT, and (c) RESI images of the investigated emitter dots-only cell at step 2 of emitter dots failure.

density and lower junction voltage. For the isolated emitter dot to receive current, the current would in fact need to travel from the still functioning emitter dots along the neighboring gridlines to the isolated dot. This path has a considerably higher series resistance with respect to the one the current would take if the dots were still functioning. This explains the considerable decrease in the activity of the isolated emitter dot, favoring a quasi-total current redistribution among the other functioning emitter dots. Current redistribution and series resistance effects explain the fact that isolated emitter dots and the area around them appear darker also in DLIT imaging, and brighter in RESI imaging, as shown in Fig. 4(b) and (c).

From these observations, it is concluded that isolated emitter dots are visible in EL and DLIT images as the emitter dots that do not show the characteristic bright halo and brightness and, conversely, as the ones that appear bright in RESI images. This conclusion is valid for any number of isolated emitter dots. In contrast, when only one emitter dot was isolated, the I_{sc}, V_{oc}, and efficiency of the device were unchanged and the FF decreased only by 0.2% abs, a smaller value than the accuracy limits of the solar simulator used. A single isolated emitter dot is therefore not detectable via *IV* tracing, whereas a single isolated emitter dot is clearly visible in EL, DLIT, and RESI images. *IV* tracing started to reliably indicate isolated emitter dots only when there were three or more of them per solar cell. This is almost a fifth of the total, which would correspond to a considerable magnitude of isolation. Even after five isolation steps, the FF only decreased by 1.8% abs and the efficiency by 0.4% abs. The I_{sc} and the V_{oc} remained unchanged.

3) Base Dots Isolation: The EL, DLIT, and RESI images of the base dots-only cell at step 4 of the sequence of base dots isolation are shown in Fig. 5(a)–(c). The black circles show the

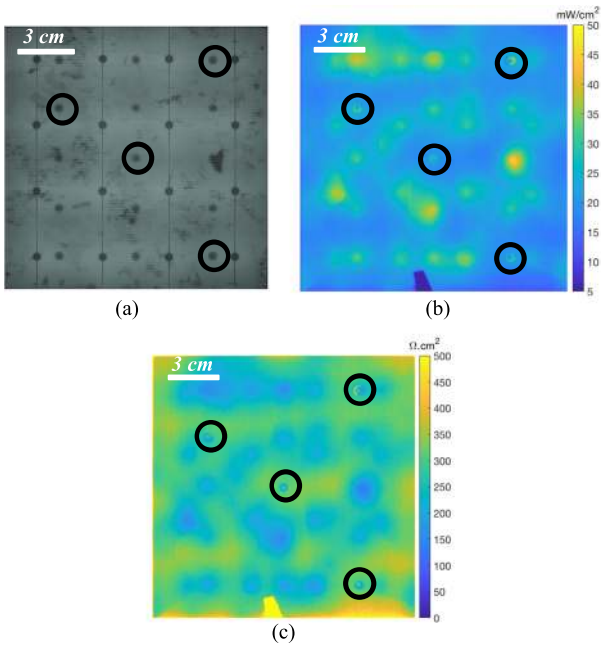

Fig. 5. (a) EL, (b) DLIT, and (c) RESI images of the investigated base dots-only cell at step 4 of emitter dots failure.

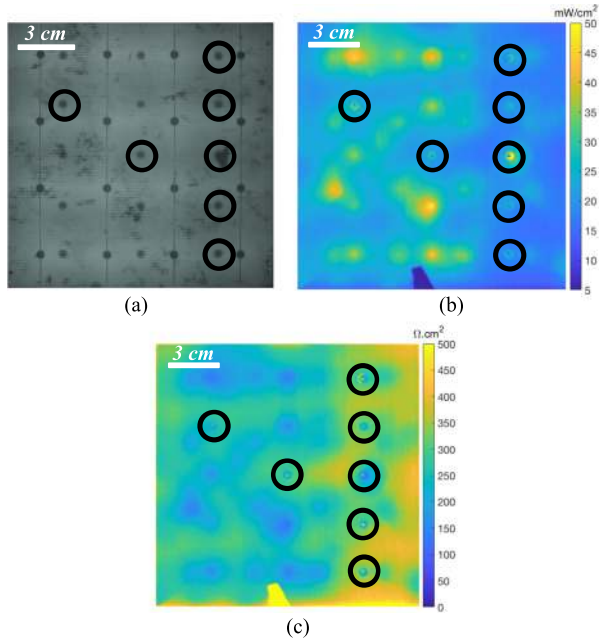

Fig. 6. (a) EL, (b) DLIT, and (c) RESI images of the investigated base dots-only cell at step 7 of emitter dots failure.

isolated base dots. In Fig. 5(a), it is observed that isolated base dots are indistinguishable from connected base dots in EL imaging. This is caused by the fact that base dots contact the Al-BSF via silver pads. The Al-BSF is a well-conducting layer spread across the whole rear area of the base layer, and the removal of a single or a low number of current injection/extraction dots causes a negligible effect on current distribution and therefore on the EL image. Current is in fact still being conducted in the area surrounding the base dots via the well-conducting Al-BSF, rather than through the dots themselves (note that this might not be the case if a thinner Al-BSF is used, in which case similar results as for the emitter dots would likely be observed). For the same reason, while base dots in DLIT images are imaged as bright spots, base dot isolation does not produce very noticeable and appreciable darkening of the area surrounding the isolated dots in DLIT images either, as can be seen from Fig. 5(b). Their isolation is instead visible as the lack of the very bright dot center that denotes functioning dots with current flowing through them, as current flow through the dot is now interrupted. Note that the brightness visible in the circled dots is an artifact due to reflection of the exposed contact and it is very sharply defined, rather than widely diffused as the brightness denoting functioning dots. Base dot isolation has a very low effect on RESI images as well, as can be seen from Fig. 5(c). Brighter areas of higher series resistance appear around the isolated base dots, but they are much fainter in brightness as the Al-BSF provides a sufficiently well-conductive current pathway to those areas, lowering series resistance losses.

Nevertheless, current conduction through the Al-BSF was only favored up until a larger number of base dots were isolated. At failure step 7 in the base dots-only cell, current redistribution to the section of the cell in direct contact with the remaining functioning base dots became most favorable. The EL and DLIT images in Fig. 6(a) and (b) picture the last step of failure in the base dots-only cell, in which a darkening of the right side of the image denotes current redistribution following isolation of the totality of the rightmost vertical row of base dots. Complete isolation of the right row of base dots is also well visible as a bright area of highly increased series resistance in the corresponding RESI image reported in Fig. 6(c). These observations are corroborated by *IV* investigations showing that isolation of one base dot decreased the FF by only 0.1% abs, with unchanged I_{sc}, V_{oc}, and efficiency. A significant lowering of *IV* characteristics was only noticed when five or more of them were isolated per solar cell. To identify base dot isolation by *IV* data, therefore, a third of the base dots had to be isolated, an even larger number than for emitter dots. Furthermore, seven isolation steps decreased the FF by only 1.4% abs and the efficiency by 0.4% abs, whereas the I_{sc} and the V_{oc} remained unchanged. Moreover, between steps 6 and 7, the FF decreased by as much as 0.6% abs, more than it decreased in the previous isolation steps, indicating that only the complete isolation of the rightmost vertical row of base dots introduced a severe performance-limiting condition. These are all smaller degradation rates than the ones caused by the isolation of the emitter dots, suggesting that the alternative current path provided by the Al-BSF is enough to counteract moderate base dot isolation.

B. Isolated Dot Identification Method

From the imaging investigations carried out in Section III-A, two automated methods for isolated contact dot identification were developed. It should be noted that both methods presented are sensitive to the degree of activity of the dots. A large degree of current redistribution due to the presence of significant defects

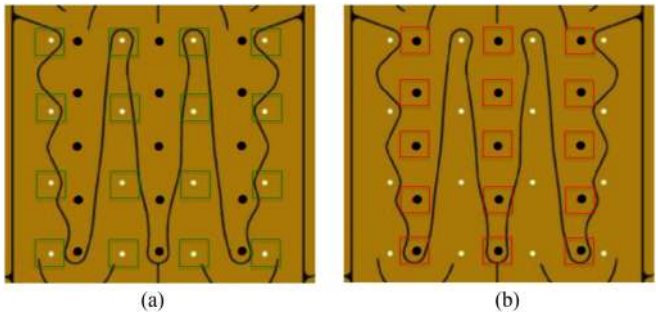

Fig. 7. Sampling locations of emitter and base contact dots. (a) Emitter dots sampling in emitter dots-only cell. (b) Base dots sampling in base dots-only cell.

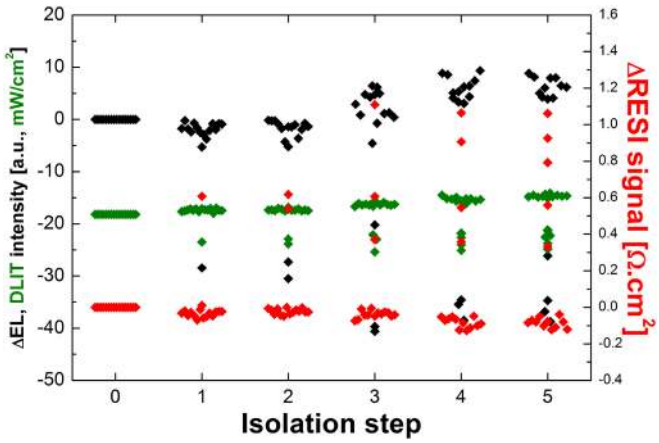

Fig. 8. Different EL (black), DLIT (green), and RESI (red) signals of emitter dots in the emitter dots-only cell.

in the vicinity of the investigated dot could incorrectly identify an otherwise functioning dot as isolated.

1) Differential Signal Method: The first method, based on the change in integrated intensity of the EL, DLIT, and RESI images for defined areas, is called the "differential signal" method. The signal emitted from each contact dots and in its immediate surroundings was sampled in all EL, DLIT, and RESI images. Fig. 7(a) and (b) show, respectively, the integration areas of emitter and base dots in the cells. The step 0 image was taken as the reference image. The differential signal of each area was then carried out by subtracting from the reference image the signal in the images of subsequent isolation steps. In case a contact dot (area) darkens, a negative differential signal is observed, whereas if it brightens, the differential signal is positive.

Fig. 8 shows the differential signal of the emitter dots at each isolation step in the EL, DLIT, and RESI images of the emitter dots-only cell. It is observed that in the EL and DLIT sets, the isolated emitter dots correspond to the ones lying well below the rest of their corresponding set, whereas in the RESI set they lay above. It can be seen that isolation can be observed when as little as one emitter dot has been isolated, making isolation detectable earlier than via *IV* measurements. It can be noted that the connected emitter dots experience a small increase in their differential signal at the later steps of isolation in the EL and DLIT sets. This is due to current redistribution within the

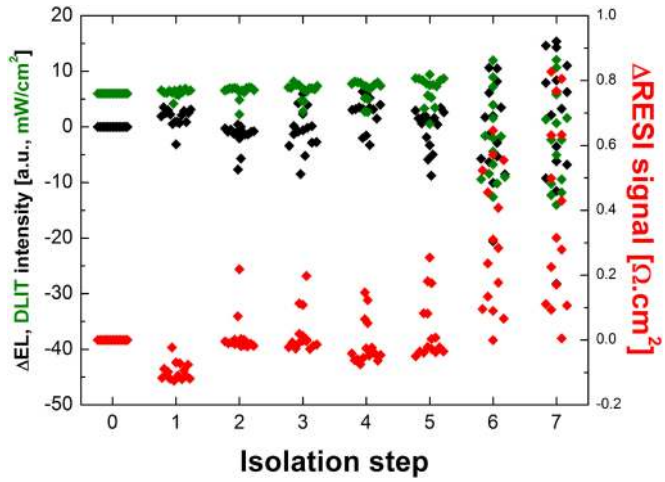

Fig. 9. Different EL, DLIT, and RESI differential signals of base dots in base dots-only cell.

cell, which causes more current to be conducted through the remaining functioning dots, thereby increasing their apparent brightness in both EL and DLIT images. Likewise, a small decrease is observed for the differential signal of the RESI sets.

Fig. 9 shows the differential signal of the base dots at each isolation step in the EL, DLIT, and RESI images of the base dots-only cell. In these sets, identification of the isolated base dots is harder. The EL set does not give any information regarding the isolation state of the base dots. This was expected, as base dot isolation could not be observed in the EL images. In the DLIT and RESI sets, on the other hand, the isolated base dots are visible as outliers with respect to the functioning base dots, but their degree by which they are outliers is very small. A reliable threshold value allowing the differentiation between functioning and isolated base dots could not be determined as a result. Moreover, the high inhomogeneity visible in the EL, DLIT, and RESI sets at the isolation steps 6 and 7 is a result of the current redistribution events that took place within the cell, previously discussed in Section III-A, further disturbing the identification of the isolated base dots.

Only emitter dot isolation is therefore reliably identifiable via this graphical method, whereas base dot isolation is harder to determine. Base dot isolation is also less of a pressing issue to identify during quality control of solar cells due to the well-conductive alternative path the Al-BSF provides to the current. This implies that an automated isolated emitter dot identification method is more useful to be set up for the emitter dots. In this paper, we propose an identification method relying on the discussed differential signal, for the derivation of which the EL, DLIT, and RESI images of a cell taken at an isolation-free time and images taken at a later time are required. This method is therefore not suitable for quality assessment immediately after the batch has been produced, but is instead suitable for quality control over extended periods of time, to monitor the state of installed modules. Quality assessment of freshly produced batches via this method can only be achieved in case the production line was able to produce very homogeneous sets of solar cells across its lifetime, for which base-case EL, DLIT, and RESI images

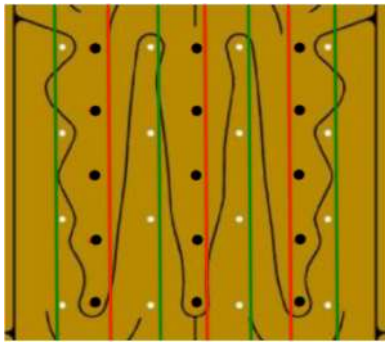

Fig. 10. Line-scanning locations of emitter and base dots.

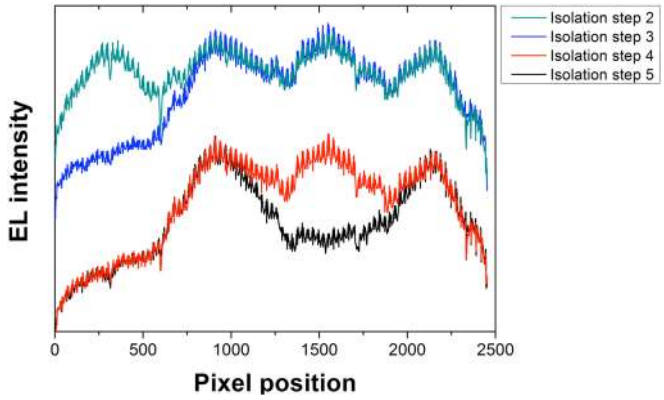

Fig. 11. EL line-scan of emitter-to-foil dots finger 4 in the emitter dots-only cell.

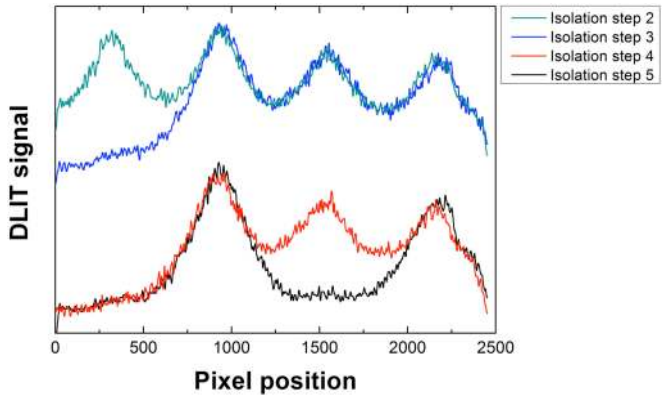

Fig. 12. DLIT line-scan of emitter-to-foil finger 4 in the emitter dots-only cell.

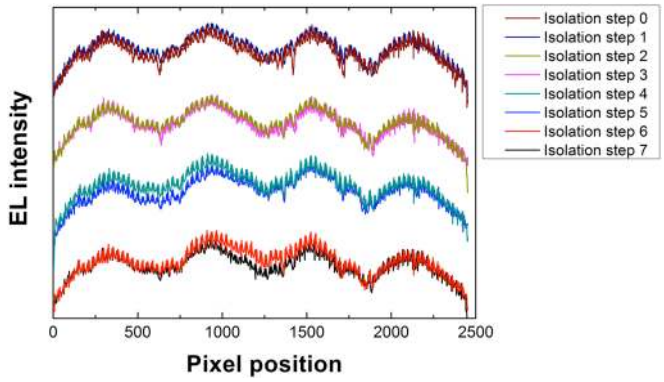

Fig. 13. EL line-scan of base dots finger 3 in the base dots-only cell.

could be used as references to derive the differential signal of each tested cell.

The presented method proposes an algorithm relying on a threshold value: Emitter dots in EL and DLIT graphs laying below it are identified as isolated, whereas emitter dots laying above it are identified as functioning. This is reversed in RESI graphs, in which the isolated emitter dots lay above the threshold value and functioning ones lay below it. The threshold value for EL graphs is –15 a.u., for DLIT graphs it is –4 mW/cm^2, and for RESI graphs it is +0.3 Ω.cm^2. Once the identification in each graph is completed, the results for each dot in each graph type (EL, DLIT, and RESI) are compared among each other. If a dot is identified by the same state (i.e., functioning or isolated) in all the graphs, the result is accepted. If the results diverge, visual investigation of the images for the specific dot is advised. This method, for the two cells investigated at each isolation step, showed a success rate of 97% for a total of 372 single dot observations (i.e., the totality of the number of readings of dots in every cell for the totality of the failure steps).

2) Line-Scan Investigation: The method outlined in Section III-B1 is affected by a key limitation: It can only be applied in cases in which a defect-free image of the specific cell is available. A reference, generic image cell cannot be used, as every cell possesses unique characteristics that influence the readings. This makes it unsuitable for the assessment of the quality of as-laminated devices. To overcome this limitation, a second identification method has been designed that only requires a single image of the cell. This method relies on EL and DLIT line-scanning and plotting of the areas adjacent the emitter and base dots, as shown in Fig. 10, where the green lines are the scan lines of the emitter dots and the red lines are the scan lines of the base dots.

Fig. 11 reports the EL line-scans of the rightmost row of emitter dots (finger 4) of the emitter dots-only cell from the second to the fifth isolation steps. It is seen in the line-scans presented in the figure that functioning emitter dots are visible as peaks at pixel locations corresponding to their position in the device, while failed dots appear as a lack of signal at their pixel location (e.g., pixel 300 at steps 3–5 and pixel 1600 at step 5). Another interesting feature are the dips, e.g., at pixel position 1750, corresponding to crystallographic defects within the cell. The noise visible all along the scan is a result of the thin front metallization fingers, which block all EL radiation. It is also worth noting that the peaks of the functioning emitter dots left at step 5 are more pronounced than in the previous steps due to current redistribution effects. The same conclusions can be drawn from the DLIT line-scan of the same area, as visible in Fig. 12. In both EL and DLIT, moreover, the magnitude of the peaks is dependent on the degree of activity of the specific dot and inequalities among the peaks of differently functioning dots can therefore be present.

Fig. 13 presents the EL line-scans of the rightmost row of base dots (finger 3) of the base dots-only cell after each isolation step. It is observed that due to the lack of halo of functioning base dots in EL images, none of the isolated base dots is visible in the line-scans, despite there being as many as five isolated

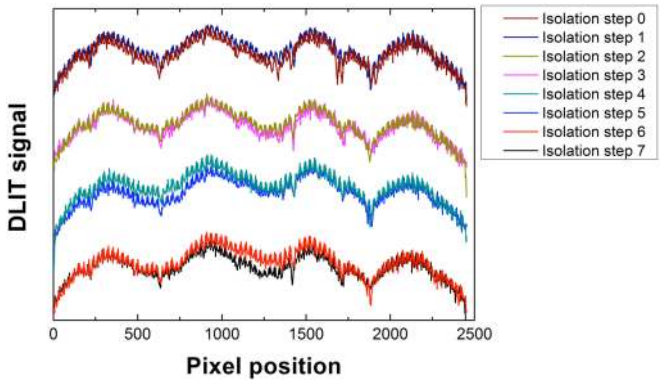

Fig. 14. DLIT line-scan of base dots finger 3 in base dots-only cell.

base dots on the same row in the last step of isolation. EL line-scans and images are instead dominated by the behavior of the emitter dots, as previously discussed. The DLIT line-scans of the same area, as shown in Fig. 14, show similar results. While base dot failure could be faintly observed by visual inspection of the DLIT images, the change in signal of the DLIT line-scan is too small to be accurately determined and, as in case of the EL line-scans, the scans are dominated by the signals of nearby functioning emitter dots.

The presented line-scan method proposes the identification of isolated emitter dots by capturing line-scans along the emitter dots fingers and identifying areas of no or low signal at the pixel positions correspondent to emitter dots in EL and DLIT images. The same procedure was applied to the base dots fingers, but isolated base dots could not be identified. Correctly functioning emitter dots show strong peaks at these locations, while isolated ones do not. The DLIT images produce line-scans with sharper and more intense peaks, owing to the fact that DLIT images are approximately proportional mappings of the locally dissipated power. They are therefore more indicated toward the implementation of this method for quality control of devices. Functioning emitter dots in EL images are on the other hand only distinguished by rather faint halos around them, translating to a lower contrast between active and inactive dots in the line-scans, which could complicate reading. The main advantage of this method with respect to the differential signal one is the fact that only a single image of the cell to be investigated is necessary. Whereas the latter method requires two images for its implementation, the line-scan method can be carried out on any arbitrary MWT solar cell, regardless of whether previous images were already captured. The line-scan method is therefore viable for implementation in the quality control protocols of as-laminated devices. Moreover, while the line-scans in this paper were visually analyzed, an algorithm automatically identifying areas of low emission correspondent to emitter dots could be easily incorporated, speeding up the process if implemented on an industrial scale.

C. Applicability to Other c-Si Solar Cells Architectures

The techniques, the considerations, and the conclusions drawn in this paper can be extended to a number of other photovoltaic technologies. Examples include breaking of metallization fingers or tabs in soldered H-pattern solar cells, but also emerging interconnection schemes like multiwire or low-temperature interconnection for heterojunction solar cells. Signal variation due to isolation should be visible in EL, DLIT, and RESI imaging. The identification method presented is not limited to Al-BSF or MWT devices and not limited to failing contact dots, but is applicable to any degradation that leads to redistribution of current that will lead to local changes and/or redistribution of EL, DLIT, and RESI signal. This methodology could be especially useful on interdigitated back-contact solar cells (IBC), as cell–cell interconnection of MWT and IBC is identical. Furthermore, three-busbar solar cells can also be investigated according to this methodology, but it might not give very useful results as any missing or poor contacts would be compensated by nearby signal (especially if the busbars are glued/soldered on the wafer along their full length). However, if more than three busbars are present and the busbars are glued/soldered only at regular intervals, the methodology becomes relevant again. This holds true also for multiwire and smartwire interconnection schemes: Failure of a few contacts with tenths wires connected at a large number of points is not an issue as such, but it could be a first indicator of degradation/failure of the cell.

IV. Conclusion

We have investigated the appearance and behavior of intentionally isolated emitter and base dots in MWT solar cells by introducing manual isolation of the dots in two devices and taking *IV*, EL, and DLIT measurements in between. Series resistance distribution images (RESI) have been derived from the EL and DLIT images.

EL images show that functioning emitter dots are visible as dots showing a bright halo surrounding them, whereas the dot and halo are lacking for isolated emitter dots. The isolation state of base dots cannot, on the other hand, be determined from EL images, as they lack the halo even when they are functioning and the Al-BSF provides a well-conducting alternative path for the current in the event of base dot isolation, minimizing series resistance losses. DLIT images show that functioning emitter and base dots show high, spreading signals, whereas isolated dots have strongly decreased signals at and around their position. The decrease in signal is more pronounced for isolated emitter dots than for isolated base dots, also in this case owing to the series resistance dampening action the Al-BSF produces for base dot isolation. In RESI imaging, areas around functioning emitter and base dots show low series resistance values, whereas areas around isolated dots show increased series resistance values. Also in RESI imaging, the isolated emitter dots show much higher brightness than isolated base dots. When a large number of clustered, isolated base dots is introduced, this leads to a significant current redistribution and large inhomogeneities in the EL, DLIT, and RESI mappings at the corresponding side of the solar cell.

Finally, the EL, DLIT, and RESI imaging methods provide a valuable tool to recognize early signals of failure within the cells that were not detectable via the collected *IV* measurements. Moreover, and most importantly, they allow the determination

of the location of failures, which is intrinsically impossible to achieve via *IV* testing.

The peculiarities and advantages of these methods over *IV* testing allowed the designing of an automated isolated contact dot identification method relying on their produced images, which could however only be reliably designed for the identification of isolated emitter dots and not for isolated base dots. These are in fact impossible to identify in EL imaging and harder to identify in DLIT and RESI imaging. Moreover, emitter dot isolation represents a more severe performance-degrading event for the cell than base dot failure.

Two automated isolated emitter dot identification methods were designed: One relying on establishing threshold values and then cross checking the differential signal for each dot; and another one relying on line-scanning next to a row of dots. The former is only applicable in case an isolation-free image of the cell is available. The latter is on the other hand applicable to any cell at any point of its lifetime, as only a single image of the cell is necessary for the investigation.

REFERENCES

[1] K. Jager, O. Isabella, A. H. M. Smets, R. A. C. M. M. van Swaaij, and M. Zeman, *Solar Energy: Fundamentals, Technology and Systems*. Delft, The Netherlands: Delft Univ. Technol., 2014.

[2] International Energy Agency, Paris, France, "2015 snapshot of global PV market," 2015.

[3] M. Chegaar, G. Azzouzi, and P. Mialhe, "Simple parameter extraction method for illuminated solar cells," *Solid-State Electron.*, vol. 50, nos. 7/8, pp. 1234–1237, 2006.

[4] J. A. Carson, *Solar Cell Research Progress*. Hauppauge, NY, USA: Nova Publishers, 2008.

[5] A. Sayigh, *Renewable Energy in the Service of Mankind Vol* II*: Selected Topics from the World Renewable Energy Congress WREC 2014*. New York, NY, USA: Springer, 2015.

[6] K. Bouzidi, M. Chegaar, and A. Bouhemadou, "Solar cells parameters evaluation considering the series and shunt resistance," *Sol. Energy Mater. Sol. Cells*, vol. 91, no. 18, pp. 1647–1651, 2007.

[7] R. Rösch, F. C. Krebs, D. M. Tanenbaum, and H. Hoppe, "Quality control of roll-to-roll processed polymer solar modules by complementary imaging methods," *Sol. Energy Mater. Sol. Cells*, vol. 97, pp. 176–180, 2012.

[8] O. Nos *et al.*, "Quality control method based on photoluminescence imaging for the performance prediction of c-Si/a-Si:H heterojunction solar cells in industrial production lines," *Sol. Energy Mater. Sol. Cells*, vol. 144, pp. 210–220, 2016.

[9] T. Trupke, *et al.*, "Photoluminescence imaging for photovoltaic applications," *Energy Procedia*, vol. 15, pp. 135–146, 2012.

[10] K. Ramspeck, K. Bothe, D. Hinken, B. Fischer, J. Schmidt, and R. Brendel, "Recombination current and series resistance imaging of solar cells by combined luminescence and lock-in thermography," *Appl. Phys. Lett.*, vol. 90, 2007, Art. no. 153502.

[11] T. Fuyuki and A. Kitiyanan, "Photographic diagnosis of crystalline silicon solar cells utilizing electroluminescence," *Appl. Phys. A*, vol. 96, no. 1, pp. 189–196, 2008.

[12] M. W. P. E. Lamers *et al.*, "17.9% metal-wrap-through mc-Si cells resulting in module efficiency of 17.0%," *Prog. Photovolt.*, vol. 20, no. 1, pp. 62–73, 2012.

[13] J. Coello, "Introducing electroluminescence technique in the quality control of large PV plants," in *Proc. 26th Eur. Photovolt. Sol. Energy Conf. Exhib.*, 2011, pp. 3469–3472.

[14] W. Yongqing, Z. Haipeng, S. Dengyuan, and C. Ailing, "Research to the typical defects of crystalline silicon photovoltaic cells based on EL images," *Int. J. Energy Sci.*, vol. 3, no. 3, pp. 200–204, 2013.

[15] T. Fuyuki, H. Kondo, Y. Kaji, A. Ogane, and Y. Takahashi, "Analytic findings in the electroluminescence characterization of crystalline silicon solar cells," *J. Appl. Phys.*, vol. 101, 2007, Art. no. 023711.

[16] J. Haunschild, M. Glatthaar, M. Kasemann, S. Rein, and E. R. Weber, "Fast series resistance imaging for silicon solar cells using electroluminescence," *Phys. Status Solidi*, vol. 3, nos. 7/8, pp. 227–229, 2009.

[17] O. Breitenstein, A. Khanna, Y. Augarten, J. Bauer, J.-M. Wagner, and K. Iwig, "Quantitative evaluation of electroluminescence images of solar cells," *Phys. Status Solidi RRL*, vol. 4, pp. 7–9, 2010.

[18] D. Hinken, K. Ramspeck, K. Bothe, B. Fischer, and R. Brendel, "Series resistance imaging of solar cells by voltage dependent electroluminescence," *Appl. Phys. Lett.*, vol. 91, 2007, Art. no. 182104.

[19] M. Köntges, M. Siebert, D. Hinken, U. Eitner, K. Bothe, and T. Potthof, "Quantitative analysis of PV-modules by electroluminescence images for quality control," in *Proc. 24st Eur. Photovolt. Sol. Energy Conf.*, 2009, Page 3227.

[20] B. Li, A. Stokes, and D. M. J. Doble, "Two dimensional mapping of electrical properties of PV modules using electroluminescence," in *Proc. 26th Eur. Photovolt. Sol. Energy Conf. Exhib.*, 2011, pp. 3285–3289.

[21] O. Breitenstein, W. Warta, and M. Langenkamp, *Lock-in Thermography - Basics and Use for Evaluating Electronic Devices and Materials*. New York, NY, USA: Springer, 2010.

[22] O. Breitenstein, "Separate imaging of space charge and bulk recombination current distribution by lock-in thermography," in *Proc. 26th Eur. Photovolt. Sol. Energy Conf. Exhib.*, 2011, pp. 1171–1181.

Edoardo Ruggeri received the M.Eng. degree in mechanical engineering from the University of Southampton, Southampton, U.K., in 2014 and the M.Sc. degree in sustainable energy technology from Delft University of Technology, Delft, The Netherlands, in 2016. He is currently working toward the Ph.D. degree in the Optoelectronics Group, Cavendish Laboratory, University of Cambridge, Cambridge, U.K., under the supervision of Dr. Sam Stranks.

His main research areas are high- and low-dimensional mixed lead-tin perovskites for photovoltaic applications and their improvement in ambient stability and optoelectronic performance.

Bas B. Van Aken is Specialist Scientist with the PV Modules and Applications group at ECN part of TNO — Solar Energy, focusing on performance, reliability, and economics of n-type bifacial and back-contact modules and bifacial PV power plants. Before, he worked on thin film Si solar cells by PECVD. After receiving a Ph.D. degree in solid state chemistry at the University of Groningen, he worked as a post-doc at Cambridge University and the Max-Born-Institute for Nonlinear and Ultrafast Optics in Berlin. His work has been published by, amongst others, *Nature, Nature Materials*, and *Physical Review Letters*.

Olindo Isabella received the Ph.D. degree (*cum laude*) from the Delft University of Technology, Delft, The Netherlands, in 2013 for his research on light management in thin-film silicon solar cells.

Between 2013 and 2017, he was an Assistant Professor with the Delft University of Technology in the Photovoltaic Materials and Devices Group. In October 2017, he was appointed as an Associate Professor in the same group, where he supervises optoelectrical device modeling activities, novel concepts of light management, development of high-efficiency solar cells based on crystalline silicon and thin-film silicon technologies, and advanced power modeling for custom PV systems.

Miro Zeman received the Ph.D. degree (*cum laude*) from the Slovak University of Technology, Bratislava, Slovakia, in 1989 for research on amorphous silicon.

In 2009, he was appointed as a Full Professor with the Delft University of Technology, Delft, The Netherlands, where he leads the Photovoltaic Materials and Devices Group and is the Head of the Electrical Sustainable Energy Department. He is a leading expert in light management, modeling, and development and application of novel materials and nanostructures in silicon-based solar cells.